Ultrastructural correlates of circadian structural plasticity

Ispizua JI*[1], Rodríguez-Caron M*[1], Tassara FJ[1], Keunyoung K[2], Insusarry Perkins C[1], Barzi M[1], Carpio-Romero C[1], Hansen CN[3], Gargiulo J[1], Rosato E[3], de la Iglesia H[4], Ellisman M[2,5], Ceriani MF[1].

[1] Laboratorio de Genética del Comportamiento. Fundación Instituto Leloir, IIB-BA/CONICET. Buenos Aires, Argentina

[2] Center for Research in Biological Systems, National Center for Microscopy and Imaging Research, University of California at San Diego, San Diego, CA, USA.

[3] Department of Genetics, Genomics and Cancer Studies, University of Leicester, Leicester, UK

[4] Department of Biology, University of Washington, Seattle, WA, USA.

[5] Department of Neurosciences, University of California at San Diego School of Medicine, San Diego, CA, USA.

*These authors contributed equally to this work.

Abstract

The central clock in the *Drosophila*'s brain consists of approximately 250 neurons organized into a relatively complex network. Within this network, four small Lateral ventral Neurons (s-LNvs) in each hemisphere are rhythmically loaded with the neuropeptide pigment dispersing factor (PDF), which plays a crucial role in synchronizing the calcium rhythms across the network. Additionally, there are daily variations in markers of active synaptic sites at their terminals, along with changes in synaptic partners. The s-LNv axo-dendritic arbor undergoes characteristic remodeling in sync with these events, a process known as circadian structural plasticity. The relationship between these various plastic changes remains unclear, largely due to a lack of techniques that offer precise, comprehensive insights into both connectivity and structure. In this study, we genetically labeled the mitochondrial matrix of the s-LNvs using APEX2 peroxidase expression, enabling us to generate three Serial Block-face Scanning Electron Microscopy (SBEM) volumes where the s-LNvs were recognizable. Each volume represents a distinct time point in the circadian remodeling of the s-LNv terminals: ZT22 (two hours before dawn), ZT2 (two hours after dawn), and ZT14 (two hours after dusk). By tracing the labeled mitochondria, we identified and segmented the terminals of four s-LNvs in each brain. We then manually

segmented dense core vesicles, both free-floating and those fusing to the membrane, as well as pre-synaptic sites and mitochondria. We discovered that dense core vesicles (DCVs) are accumulated and released from the s-LNv varicosities with a peak in the morning. Additionally, we observed nearly 50% more presynaptic sites in the morning compared to nighttime. These changes are accompanied by a marked shift in mitochondrial shape and volume, indicating functional differences between day and night. Finally, these adjustments are coordinated with changes in neurite length and the number of varicosities. We propose that structural plasticity helps organize daily changes in functional units, dynamizing the impact of these neurons on the network.

Introduction

Life has always been subjected to variations in environmental conditions due to Earth's translation and rotation. The selective pressure of these peaks and troughs favored the emergence of molecular strategies that allowed organisms to anticipate environmental changes and adapt their physiology in advance[1,2]. One of such strategies is the surge of circadian clocks. These clocks dictate the optimal times to eat, move, express genes, photosynthesize or mate. In *Drosophila*, it ticks inside a network of nearly 200 neurons in the central brain[3], which is capable of great plasticity in terms of response to sudden changes in environmental conditions[4], neuropeptide expression[5–7], and even changing the roles and hierarchy between neuronal clusters when one of them is genetically manipulated or eliminated[8,9].

Within *Drosophila's* clock, the small Lateral ventral Neurons (s-LNvs, only four per hemisphere) express the Pigment Dispersing Factor (PDF) neuropeptide[10], necessary to maintain rhythmic behavior under typical laboratory free-running conditions[8,11–13]. The s-LNv processes in the dorsal protocerebrum exhibit an arborization pattern that undergoes stereotyped changes throughout the day[14]. This intriguing form of adult neuronal plasticity results in more complex terminals in the morning and less so at night. Such structural remodeling occurs concurrently with other plastic events. On the one hand, the peak in PDF immunoreactivity coincides with the maximum spread of the s-LNv dorsal terminals[6]. Furthermore, the number of synapses, as indicated by the expression of a fluorescent marker of active zones, also reaches its peak at the time of maximum complexity[15]. These properties similarly respond to changes in excitability[16–18]. This comparable daily pattern indicates that these processes are intertwined. Nevertheless, a comprehensive characterisation of the underlying cellular phenomena through fluorescent reporters and confocal fluorescence microscopy remains a significant challenge, particularly in

light of the potential for unintended consequences associated with the modification of tightly regulated and spatially constrained molecules, such as synaptic or vesicular ones.

In this work, we address the question of how all these phenomena are interconnected by employing volumetric electron microscopy (EM). We established a method for precisely labeling neuronal mitochondria for further cell identification and created a semi-automated convolutional neural network (CNN) to facilitate future work. We processed three female volumes, one for each milestone remodeling timepoint: ZT22 (two hours before dawn), ZT2 (two hours after dawn), and ZT14 (two hours after dusk). After creating a manually-segmented model of four s-LNvs, we identified dense core vesicles, both free and fusing, presynaptic sites and mitochondria. Thus, we found that DCVs accumulate and release their content from the s-LNv varicosities with a peak in the morning. This observation was subsequently validated through the development of a genetic tool to assess DCV fusion with the membrane, designated GRIP (GFP reconstitution in the pre-synapse). Additionally, we observed nearly 50% more presynaptic sites in the morning compared to nighttime. Similar to the DCVs, the presynaptic sites are also concentrated within the varicosities. These changes are accompanied by a marked shift in mitochondrial shape and volume, indicating functional metabolic differences between day and night. Finally, these adjustments are coordinated with changes in neurite length and the number of varicosities. We propose that this plasticity dynamically modulates the influence of the s-LNvs onto the circadian network, orchestrating daily fluctuations in the number and strength of functional units.

Results

Mitochondrial labeling allows rapid segmentation of *Drosophila* neurons in 3D EM volumes

To investigate circadian structural plasticity at the ultrastructural level and thus define the nature of the structural changes occurring as a result, we generated 80x80x100 µm electron microscopy volumes containing the s-LNv terminals by Serial Block-face Scanning Electron Microscopy (SBEM). To guide the identification of the neurons of interest we took advantage of the differential expression of the peroxidase APEX2[19], which reacts with diaminobenzidine (DAB) to generate differential contrast in cell membranes. To prevent that excess labeling impairs the identification of fine structures at the plasma membrane, we generated a novel fly reporter line targeting APEX2 to the mitochondrial matrix; in addition, APEX2 was fused to the fluorescent protein mKO2 for correlated light and electron microscopy (the resulting construct is

UAS-mito::mKO2::APEX2, hereinafter mito-APEX2). We used micro-computed tomography (micro-CT) correlated with confocal images of the region of interest prior to *en-bloc* staining to identify the region of interest. We chose three time points coinciding with the times of day that show the most dramatic structural changes: early morning (*zeitgeber* time 2 (ZT2)), early night (ZT14) and late night (ZT22). Briefly, ZT2 shows maximum spread, ZT14 shows minimum spread and ZT22 shows more retracted terminals[15]. One volume per time point was produced using SBEM (**Figure 1a**). Female brains were used for comparison to existing connectomes [20,21]. Differentially stained mitochondria (arrowheads, **Figure 1b**) allowed the manual segmentation and the generation of the models included in **Figure 1c** through IMOD[22]. A direct comparison of the segmented neurons with the corresponding confocal images provides compelling evidence that the former correspond to the s-LNvs (**Suppl. figure 1**). Using the data from ZT2 and ZT14, we trained a semantic classificator to recognize and segment cells containing stained mitochondria, which extremely reduces the burden of segmentation for future work (**Suppl. figure 2**).

The ability to identify individual neurons enabled a quantitative description with unparalleled detail, resulting in the observation that the number of primary, secondary and tertiary neurites remains relatively constant. Conversely, neurites tend to be longer at ZT2, which, coupled with the observation of more numerous boutons (small sprouts, **Figure 1d**), contributes to the more complex morphology that is typical of the early morning structure. In addition, the overall volume of the late-night structure is notably reduced (**Figure 1e**). We confirmed that the varicosities along the neurites function as *en passant* boutons, concentrating all elements required for communication (mitochondria, dense core vesicles, pre-synaptic sites), as already hinted in foundational fly TEM papers[23]. In the remainder of the manuscript, quantitations were conducted using varicosities as the unit of analysis.

Daily changes in vesicle fusion underlie differential neuropeptide release

Dense core vesicles (DCVs) carry neuropeptides from the soma to the neuronal terminals. PDF and sNPF are the main neuropeptides produced by the s-LNvs, which among a variety of additional functions, synchronize activity in the clock network and contribute to the regulation of sleep, respectively[10,24,25]. Using the manually segmented EM models for the s-LNvs, we identified both free DCVs and those that had entered the release pathway (fused DCVs, fDCVs). This analysis showed that there is a striking difference in the DCV content and DCV release sites as a function of time of day (**Figure 2 a-f**). The overall number of DCVs and fDCVs per volume unit (DCV and fDCV density, **Figure 2 b and e**) is higher in the early morning when

compared to the night. However, at ZT22, fDCVs increase dramatically, perhaps as a result of increased excitability expected around dawn[26]. The number of free DCVs per varicosity is higher in the morning compared to ZT14 and 22. Differences between the latter only become significant in the most distal portion of the terminals. The number of fDCVs, albeit smaller, is also higher in the early morning, although towards the end of the night the amount increases in the more proximal portion of the terminals while the most distal ones show significantly higher numbers in the morning (**Suppl. Figure 3 a and b**), perhaps as a result fDCV density increases at ZT22. This suggests that DCV release is a function of the amount of DCVs available. Interestingly, fDCVs tend to be excluded from pre-synaptic densities, as previously reported[7].

To further confirm there is circadian regulation of neuropeptide release we designed a new fluorescent reporter of DCV fusion based on GFP reconstitution in the pre-synapse (that we termed GRIP). Briefly, a portion of the non-fluorescent split GFP was targeted to the DCVs (UAS-Synaptotagminα::GFP_{11}) while the other portion of the split GFP was tethered to the extracellular domain of a transmembrane carrier protein (UAS-CD4::GFP_{1-10} [27]). The concomitant expression of both fragments in PDF neurons enabled the use of reconstituted GFP fluorescence as a proxy of DCV fusion (**Figure 2g**). As described for the EM dataset, most of the fluorescence is located within the varicosities (**Figure 2h**). Notably, DCV fusion peaks early in the morning, reaching a minimum at the beginning of the night, and increases again towards the end of the night (**Figure 2 i and j**), confirming observations made through SBEM in single volumes (**Figure 2e**). Altogether these results suggest a time of day dependent differential neuropeptide availability and release.

Presynaptic sites are more abundant in the morning

Synaptic sites are trans-cellular structures that organize fast neurotransmission between neurons. At the pre-synaptic site, scaffold proteins nucleate clear vesicles and release them after a depolarization event. Pre-synaptic densities can be detected in the SBEM images (**Figure 3a**, model and arrowheads). They are reminiscent of T-bars, surrounded by dense accumulations of unresolved clear vesicles. The majority of the synapses, if not all, are polyadic and situated almost exclusively in varicosities and boutons (**Figure 3a**, right panel, asterisks). Following a careful manual segmentation process, it was observed that the morning structure exhibited a twofold increase in pre-synaptic sites in comparison to the volumes obtained at night (**Figure 3b**). Significant differences in the number of active zones per varicosity were only discernible in the most distal region of the terminals (**Figure 3c, Suppl. Figure 3c**). On the other hand, presynaptic density (number of presynaptic sites per unit volume) decreases at the

beginning of the night and then increases towards ZT22 due to the decrease in neuronal volume that occurs at this time (**Figure 3d**). Thus, differences in presynaptic connectivity are mainly due to the addition and loss of varicosities.

Dynamics of mitochondrial shape and number underlie circadian structural plasticity

Mitochondria are dynamic organelles that exist in a fused-fragmented equilibrium. In extremely polarized cells, like neurons, they have fixed positions close to synaptic site[28]. They provide energy and serve as a Ca^{2+} reservoir[29]. In the s-LNv terminals, we found that there are marked time-of-day differences in mitochondrial number and morphology (**Figure 4a**). To begin with, the volume occupied by mitochondria is slightly higher in the morning (ZT2) compared to the night (ZT14-22, **Figure 4b**). Furthermore, the volume acquired at ZT2 contains small and rounded mitochondria, usually more than one per varicosity (Figure 4a, left panel). On the other hand, there seems to be a transition towards more fused and elongated structures at the end of the night, as evidenced by a higher mitochondrial complexity index (**Figure 4c**), a parameter that approaches 1 as the shape of the object becomes rounder. Given that this is a dynamic process, it can be inferred that during the four-hour interval between ZT22 and ZT2, the elongated mitochondria would undergo fission. No correlation was observed between mitochondrial shape and the distance of the mitochondria from the point of origin of the arbor (**Suppl. Figure 3d**).

Varicosities are plastic along the day

s-LNv varicosities are membrane enlargements of the neurites of approximately 1.8 µm in diameter that gather presynaptic sites and function as fusion hubs for DCVs carrying neuropeptides (**Figure 5a**). Our results showed that the total number of varicosities per neuron was higher in the morning than in the night samples. However, the differences are not evenly distributed, with the medial and distal parts of the volumes taken at night showing the greatest differences (**Figure 5b**). Moreover, the girth of the varicosities drops dramatically toward the end of the night (**Figure 5c**) while the distance between varicosities remains stable throughout the day (**Figure 5d**), implying that new varicosities are added to the structure at regular intervals. Given that varicosities are a structural feature with a functional role, it is possible that they represent a link between structural remodeling and functional plasticity.

Discussion

Generation of machine learning algorithms to guide the segmentation

Volumetric electron microscopy is the most effective method for achieving high resolution in biological imaging, generating extensive datasets from intricate three-dimensional samples. The application of technologies such as SBEM, Single Slice Transmission Electron Microscopy (ssTEM), and Focused Ion Beam Scanning Electron Microscopy (FIB-SEM) to neural tissue has led to the establishment of the field of *Drosophila* connectomics, thereby facilitating the acquisition of new insights into neuronal circuits[20,21]. The creation of these datasets is an extremely time-consuming process, often spanning years, due to the vast scale of the data, particularly in terms of the number of neurons and synapses involved[21]. To gain a more comprehensive understanding of neural circuits across different states, it may be beneficial to examine smaller, targeted brain areas. However, even this approach requires extensive data processing. The conversion of raw data into actionable information, which involves the segmentation of structures of interest, remains a highly labor-intensive process. This necessitates the engagement of either costly specialized contractors or a large, dedicated team. To ascertain the identity of a cell, it is often necessary to process extensive volumes of data, given that identity is determined by morphology. This results in increased costs, data storage requirements and processing times. In this study, we developed a combination of an established marker (mito-APEX2) with a new informatic interface with the objective of significantly reducing the processing load of 3D-EM data (**Suppl. Figure 2**). The mito-APEX2 marker, when used in concert with either the Gal4 or LexA expression systems, enables cell-specific targeting while circumventing the considerable opacity associated with membrane-bound APEX2, which has the potential to obscure synaptic sites and other fine ultrastructural features. Furthermore, it is possible to identify a cell without having to produce a volume that encompasses it entirely. This enables the reduction of the area of interest to specific zones of interest. Two manually segmented volumes (ZT2 and ZT14) were employed to train a semantic classification network to recognize labeled mitochondria. This resulted in the development of models for both the mitochondria and the neurons that contain them. Furthermore, an algorithm utilizing convolutional neural networks was developed for the additional segmentation of DCVs. In addition, we have developed a staining protocol that ensures uniform labeling with a high signal-to-noise ratio. Together, these advances provide a streamlined and accessible pipeline for 3D-EM volume generation, expanding the potential of EM and connectomics to address

specific biological questions.

Circadian control of vesicle transport and release

Neurons use neuropeptides to convey messages that extend beyond individual synapses, producing broader metabolic changes compared to the membrane potential shifts typically induced by classical neurotransmitters[30]. The s-LNvs produce at least two types of neuropeptides, both composed of short amino acid chains: PDF and sNPF (short neuropeptide F). PDF is received by nearly 50% of the circadian network and certain non-circadian groups, such as the lamina neurons[31], triggering an increase in cyclic AMP levels. This increase appears to modulate the phase of calcium oscillations across the network[25]. Conversely, sNPF seems to promote sleep cycle consolidation by inhibiting the large ventrolateral neurons (l-LNvs), a group of clock neurons whose activation promotes wakefulness[32]. Both neuropeptides are transported within dense-core vesicles (DCVs) to the dorsal terminals of the s-LNvs, where they are captured until release[33].

Since the early 2000s, it has been known that PDF levels cycle in a circadian manner, peaking in the morning within the dorsal terminals of the s-LNvs[6]. However, the dynamics of neuropeptide accumulation and release have only been analyzed indirectly through fluorescent protein fusions with exogenous peptides[34]. The current study highlights the circadian nature of DCV accumulation within the dorsal terminals of the s-LNvs. We observe that free DCVs accumulate almost exclusively within the s-LNv varicosities, surrounding the mitochondria. Our data further shows that this accumulation decreases significantly at night, especially in the distal varicosities. A similar pattern is observed in DCVs undergoing fusion with the plasma membrane.Fusion predominantly occurs within the varicosities and exclusively outside the presynaptic densities, a pattern also proposed using fluorescent markers and expansion microscopy techniques[7]. Furthermore, we demonstrate that, similar to free DCVs, there are significantly more fusion events during the morning compared to nighttime, with the effect being more pronounced in distal varicosities. The detection of fused DCVs at nighttime indicates that, despite the majority of peptide released from the s-LNv terminals is expected at dawn -associated to the higher frequency of bursts of action potentials, these neurons still release neuropeptides at night, accompanying the circadian variation in firing frequency[35,36]. This was further confirmed in acutely fixed brains through GRIP. The reconstituted (non amplified) GFP signal was mainly restricted to varicosities, and the degree of fusion at the time-points examined (judged by GFP intensity) closely resembles the EM data. In fact, a similar daily pattern was

previously described employing a fluorescent DILP chimera at the s-LNv dorsal terminals, further confirming there is temporal control of DCV release[37].

Interestingly, distal varicosities demonstrate the greatest degree of plasticity in terms of the number of DCVs they can accommodate. Both the number of free and fused vesicles varies in a similar phase. This indicates that circadian modulation is likely to affect vesicle transport towards the dorsal projections, and that the number of vesicles fusing to the membrane may be contingent upon their availability, at least in part. A clear example supporting this hypothesis involves a s-LNv neuron observed at ZT22, where the primary neurite, after extending towards the midbrain, loops back into the axonal tract. This creates two varicosities, one proximal and one distal, separated by less than 2 μm. If the release sites were the primary determinants dictating the amount of vesicle fusion, both varicosities would behave similarly. However, the distal varicosity contains fewer DCVs and, consequently, significantly fewer vesicles fusing with the membrane compared to its proximal counterpart.

The morning structure is more closely integrated with the network

Chemical synapses are structures that organize communication between neurons. The presynaptic neuron fuses vesicles filled with classical neurotransmitters (small molecules such as acetylcholine, glycine, or glutamate), and the postsynaptic cell receives and interprets these neurotransmitters via membrane receptors, which induce downstream changes in membrane potential. In electron microscopy images of the *Drosophila* nervous system, presynaptic sites appear as clusters of clear vesicles (CVs) organized around a T-bar structure formed by scaffold proteins, whereas postsynaptic sites only exhibit a slightly darker contrast in the membrane adjacent to the synaptic cleft[23,38]. Upon segmenting these structures in our volumes, we first observed that most synapses are polyadic, meaning that a single presynaptic density is associated with multiple postsynaptic neurons, consistent with previous observations[20,23]. Another interesting observation is that these synapses are primarily organized within varicosities, with the number of presynaptic sites per varicosity remaining largely stable throughout the day; there is a tendency, however, for varicosities to exhibit fewer presynaptic densities at night, especially in the distal regions, where the differences become statistically significant. In any case, the morning structure displays approximately 50% more presynaptic sites than the two volumes taken at nighttime, a finding that is consistent with previous reports analyzed through fluorescence microscopy[15].

Mitochondrial dynamics implies changes in energy demand or specification

In each varicosity, vesicles and presynaptic sites are organized around one or more mitochondria. Given that both vesicle fusion and material transport to these structures rely on ATP, the organization of these structures into functional units appears to facilitate a localized ATP supply, thereby supporting essential communication processes. A recent study on mitochondrial morphology across the hemibrain demonstrated a correlation between mitochondrial shape and the identity of neuronal processes. Specifically, dendrites were observed to contain elongated mitochondria, while axons exhibited smaller, rounder ones[39]. This observation, coupled with prior evidence suggesting an increase in dendritic markers at the dorsal protocerebrum at night [40,41], and even enhanced responsiveness to partner activation[41], the increase in mitochondrial complexity at night may be indicative of a transition from “axonal” to “dendritic” terminals.

An alternative hypothesis would posit that changes in mitochondria morphology may indicate a differential response to stress. Just before dawn, the s-LNvs begin to fire at higher frequencies[26], accompanied by increased recruitment and fusion of DCVs and a rise in active sites requiring energy. This high demand could then stress the mitochondria, resulting in the fragmented, rounded forms observed at ZT2. Conversely, at night, as neuronal activity decreases, mitochondria tend to fuse into larger, elongated structures with reduced total surface area. This configuration may enable collective evaluation of mitochondrial “health” and membrane potential equalization[42], preparing the mitochondria for another round of metabolic stress at the start of the day.

In mammals, some evidence suggests that the circadian clock controls the abundance and morphology of mitochondria by regulating biogenesis, fission/fusion and mitophagy (reviewed in de Goede *et al* 2018[43]). Along those lines, the reduction in overall mitochondrial volume at the outset of the night may be indicative of the clearance of damaged mitochondria through the process of mitophagy. While electron microscopy images are unable to capture movement, observations of elongated mitochondria outside varicosities at night suggest that dismantling may be a potential contributing factor to the reduced complexity observed during this period.

Varicosities changes links structure to function

Circadian structural plasticity was initially described through Z-axis projections derived from confocal microscopy images of brain samples collected at different time points.Thus, changes in complexity were characterized as variations in the number of crossing processes at different distances from the centroid using Sholl analysis[44], later on, differences were defined by an image analysis algorithm [40]. Hypotheses regarding the types of subcellular changes underlying

oscillations in complexity included the growth/disappearance of new neurites, the extension/retraction of existing neurites, and changes in the degree of fasciculation (i.e., proximity between neurites)[14]. However, distinguishing between these processes requires identifying individual neurites, an impossible task given the resolution of immunohistochemistry coupled to confocal fluorescence microscopy. While random labeling of individual neurons could potentially circumvent this limitation, these labeling strategies not only exhibit low efficiency within the s-LNvs but also do not consistently label the same neuron[45].

Our data so far suggests that the number of neurites is similar across the three time points analyzed: in general, each neuron has one or two secondary neurites and only a few show tertiary neurites. Hence, changes in structural complexity would depend primarily on the growth/retraction (length) of individual neurites rather than increased branching, together with the generation of new boutons. Moreover, although some regions in the morning appear less fasciculated, no differences were detected. Given the subtle nature of these changes, they are likely obscured by inherent structural differences across time points and the limited number of observations achieved with this level of resolution.

Interestingly the high-resolution technique employed herein enabled the identification of additional changes. One such change was related to volume, whereby terminals occupied a greater space in the morning compared to the night, reminiscent of what was described in the L2 lamina neurons[46]. Another change was observed in the number of varicosities. This novel finding reveals a new dimension of circadian remodeling as it demonstrates that structural changes involve not only alterations in size or complexity, but also the addition of new, larger varicosities containing new synapses and peptide release sites.

Materials and methods

Fly rearing

Flies were grown and maintained at 25°C in vials containing standard cornmeal yeast agar medium under 12:12 h light:dark (LD) cycles. Adult-specific Gal4 expression for the GFP reconstitution experiments was achieved through GeneSwitch[16]. GeneSwitch expression was induced transferring 2- to 5-days-old flies to vials containing food supplemented with RU486 (mifepristone, Sigma, USA) in 80% ethanol to a final concentration of 200 µg/ml for exactly 72 h prior to dissection. The *pdf*-GeneSwitch (*pdf*-GS) and the mito::mKO2::V5::APEX2 described in this manuscript) lines were generated in our laboratory. *pdf*-Gal4 was obtained from the Bloomington Stock Center and *pdf*-RFP was generously provided by J. Blau (NYU, USA).

Stocks for GRIP were generated in the Rosato Lab and UAS-CD4::GFP_{1-10} was provided by K. Scott (UCBerkeley, USA).

Generation of transgenic lines

The mito::mKO2::V5::APEX2 sequence was provided by the Ellisman Lab[19]. A Kozak sequence was added upstream of the mito::MKO2::V5::APEX2 fragment. This sequence was synthesized and cloned into pJFRC81-10XUAS-IVS-Syn21-GFP-p10 (Addgene, USA) by GeneScript (GeneScript, USA), replacing the GFP coding region. Transgenic lines were produced by BestGene (BestGene, USA) by Phi31 site specific transformation into attP2 (third chromosome) or VKO2 (second chromosome) sites.

For GRIP analysis, the GFP_{11} fragment was fused through a flexible linker to the N-terminus end (pointing to the lumen of vesicles) of Synaptotagminα (Sytα). The DNA sequences encoding the fusion proteins were cloned Xho I-Xba I into pUAST[47]. Transgenic lines were produced by the University of Cambridge Fly Facility (UK) using p-element transformation. Lines expressing split GFP components in the plasma membrane (UAS-CD4:GFP_{1-10}) were already available and described[48].

GFP reconstitution in the pre-synapse (GRIP)

pdf-GS > *pdf*-RFP;GRIP flies were induced in RU for 72 h as described above. At ZT2, ZT14 and ZT22, males and females were briefly anesthetized on ice and their brains dissected in cold PBS under red light. Dissected brains were fixed in PFA 4% for 1 h at room temperature in darkness. Samples were washed in cold PBS for 15 minutes and then rinsed for 5 minutes. Finally, brains were mounted in Vectashield (Vector Laboratories, USA) with their dorsal surface upwards to allow access to the dorsal protocerebrum. Z-stacks of the s-LNv dorsal projections were taken immediately using a confocal microscope Zeiss LSM 880 (Zeiss, Germany) with Zen software.

Brain preparation for Correlative Light Electron Microscopy

Briefly, 2- to 4-day old female flies expressing *pdf*-GAL4>mito-APEX2;*pdf*-RFP were ice-anesthetized and decapitated at the corresponding time points. Heads were fixed in 2.5% glutaraldehyde and 2% paraformaldehyde in 0.15 M cacodylate buffer (CB, pH 7.4) on ice for 1 h. After removing the fixative, brains were dissected in fresh 0.05 M CB and washed 3 times for 10 min in the same buffer solution. To facilitate the penetration of the staining, an optic lobe was removed using fine forceps, leaving the adjacent region of interest undamaged. Brains were

transferred to a coverslip and imaged at 20x, 40x, and 60x in a Leica F1000 confocal microscope (LEICA,Germany). Immediately after, brains were treated for 15 min with 20 mM glycine in 0.15 M CB on ice, to quench any unreacted glutaraldehyde. For the DAB reaction, a preincubation step was done in 2.5 mM DAB solution (25.24 mM stock in 0.1 M HCl) in 0.15 M CB for 15 min on ice. For staining, 0.03% H_2O_2 containing DAB solution was added to the brains on ice for 40 min. The staining buffer was washed off with ×5 washes using 0.05 M CB. Then, brains were individually placed inside glass vials into 0.5% OsO_4 in 0.05 CB for 40 min at 4°C. Next, the OsO_4 solution was removed and, without washing, a reduced solution of 0.8% potassium ferrocyanide in 0.05 M CB containing 2 mM $CaCl_2$ was added. Brains were incubated for 2 h at 0°C. After thorough washing 3 x 10 min witn double distilled water, brains were placed into 0.5% aqueous uranyl acetate for 30 min at 4°C. Brains were washed with ddH_2O at RT 3 x 10 min and then stained with 0.05% lead aspartate solution for 4 h at 22°C or ON at 4°C. Brains were washed with ddH2O at RT 3 x 10 min and transferred to a solution of OsO_4 0.8% in 0.05 M CB for 20 min at 4°C. The brains were washed 3 x 10 min on ddH_20. Brains were dehydrated in crescent percentages of ethanol and finally to a staining solution at specific temperatures and precise intervals, by using a freeze substitution chamber (Leica AFS, Leica). Brains were individually transferred to small baskets and incubated as follows:

Temperature	1°C to -5°C	-5°C to -10°C	-10°C to -15°C	-15°C to -20°C	-20°C to -25°C	-25°C	-25°C	-25°C to 22°C
Solution	10% EtOH	30% EtOH	50% EtOH	70% EtOH	80% EtOH	90% EtOH	97% acetone 0.2% UA 1% OsO_4	97% acetone 0.2% UA 1% OsO_4
Time	20 min	20 min	20 min	20 min	20 min	20 min	33 hs	6 hs

Brains were then washed twice with dry acetone and placed into 50:50 Durcupan ACM:acetone overnight. Brains were transferred to 100% Durcupan resin overnight. Brains were then embedded in tin containers and left in an oven at 60°C for 72 hr. To proceed with Micro-computed tomography and SBEM, brains were carefully trimmed, leaving the minimum resin, and then attached to a metallic pin.

Micro-Computed Tomography, definition of the region of interest and Serial Blockface Scanning Electron Microscopy

The Micro-Computed Tomography (Micro-CT) tilt series were collected using a Zeiss Xradia 510 Versa (Zeiss X-Ray Microscopy) operated at 80 kV (87 μA current) with a 20X magnification and 0.3836 μm voxel size for ZT2, 0.4687 μm voxel size for ZT14, and 0.4688 μm voxel size for ZT22. Micro-CT volumes were generated from a tilt series of projections using XMReconstructor (Xradia). Since no visible signal from the DAB deposition was seen in the Micro-CT, neuroanatomical features such as the alpha lobe of the mushroom bodies and the protocerebral bridge were used to correlate the computed tomography data to the confocal images. A 80*80*100 μm region of interest (ROI) containing the s-LNv terminals was defined for each timepoint. SBEM was accomplished using GeminiSEM 300 (Zeiss, Oberkochen, Germany) equipped with a Gatan 3View system and a focal nitrogen gas injection setup. This system allowed the application of nitrogen gas precisely over the blockface of the ROI during imaging with a high vacuum to maximize the SEM image resolution, as described in Deerink *et al* 2017[49]. Images were acquired in 2.5 kV accelerating voltage and 1 μs dwell time; Z step size was 50 nm; raster size was 16k × 14k for ZT2, 20k × 20k for ZT14 and 20k × 24k for ZT22 Z dimension was ~900 to 1500 image samples. Volumes were collected using 90% nitrogen gas injection to samples under high vacuum. Once volumes were collected, the histograms for the slices throughout the volume stack were normalized to correct for drift in image intensity during acquisition. Digital micrograph files (.dm4) were normalized and then converted to MRC format. The stacks were converted to eight bits and volumes were manually traced for reconstruction using IMOD[22]. The s-LNvs were identified as neurons containing labeled mitochondria. They were segmented starting 2 microns below the first ramification of the first branching neuron of the bundle. DCVs were identified as dense, round structures of 90-200 nm. When connected to the plasma membrane, DCVs were marked as fusing DCVs. Synaptic sites were identified as a high electron density spot in the membrane with at least 2 post-synaptic partners, where a cloud of clear vesicles or a t-structure was deposited. These three elements were segmented as scattered objects. Mitochondria were recognized by shape, matrix pattern and high contrast due to DAB staining, and segmented as closed objects. Following the segmentation process, a single round of independent manual proofreading was conducted. The data pertaining to the total number of scattered objects, neuronal and mitochondrial volume, and surface area were extracted using the *-imodinfo* command. Quantification was initially performed on a per-varicosity basis, with the varicosities themselves first defined and then the objects within the model counted. For the purposes of quantitation per zone, the primary neurite on each neuron was defined as the longest path from the point of origin of the structure. Subsequently, the relative position of each varicosity within a given neuron was normalized in relation to the length

of the primary neurite of that neuron. Secondary neurites were defined as the longest protrusion emerging directly from a primary neurite. Tertiary neurites were defined as protrusions from secondary neurites. Boutons were defined as small sprouts containing just one varicosity. The MCI was calculated using the equation described by Vincent *et al* 2009[50]:

$$MCI = \frac{mitochondrial\ surface^3}{16 \times mitochondrial\ volume^2 \times \pi^2}$$

Semi automated segmentation

Three main neural networks support the tool's segmentation tasks. Firstly, a semantic segmentation model identifies s-LNv terminals by detecting stained mitochondria, which is then followed by a high-precision model that refines the boundaries of the mitochondria. A convolutional neural network (CNN) is employed for the detection of vesicles within the boundaries of neurons. The segmentation models utilize Residual Attention U-Net on small patches (6.4 x 6.4 µm) to optimize efficiency, subsequently reassembling the patches to facilitate full volume segmentation. Neuron and mitochondrial annotations from previous IMOD data, refined in Python and ImageJ, provided ground truth for training on 4,150 images.

For vesicle detection, a "mobile classifier" (developed by PyTorch) uses a CNN[51] with four layers, max-pooling, and fully connected layers on 250 x 250 nm patches to estimate the probability of vesicle presence. A second "refinement classifier" is employed to reduce the number of false positives, utilizing larger 500 x 500 nm patches to provide greater context around vesicle centers. The classifiers were trained and validated on a dataset comprising thousands of vesicle and non-vesicle images.

Finally, using py-clesperanto[52] for GPU-accelerated 3D segmentation, each structure is labeled to facilitate metric calculations, like structure count and distribution within the volume.

Quantification and statistical analysis

The statistical analyses were performed using the R software, version 4.1.0. General and mixed linear model analyses were conducted using the *nlme* package (v. 3.1-164[53]). For generalized linear mixed models, the data were initially fitted to a Poisson distribution using the *lme4* package (v. 1.1-35.5[54]). In instances where overdispersion assumptions were not satisfied, a negative binomial distribution was employed using the *glmmTMB* package (v. 1.1.10[55]). One- or two-way ANOVA were performed if a general linear model was applied, and Wald chi-square test was done in generalized linear models. For post hoc comparisons, the *emmeans* package (v. 1.10.5[56]) was employed, with Bonferroni corrections applied.

Dense core vesicles (DCVs), fusing DCVs, and presynaptic sites per varicosity. A model was applied to each neuronal region and each object. Generalized linear mixed models with a Poisson distribution were fitted, with neurites considered as a random effect. In cases where the assumptions were not met (overdispersion), a negative binomial distribution was used.
An additional analysis was done to compare interactions between distance to the first branching site and the time point and post hoc analysis was performed with the Bonferroni test.
GFP reconstitution in the pre-synapse. GFP signal in the dorsal projections of s-LNvs was quantitated using ImageJ (NIH). Maximum intensity Z projection of *pdf*-RFP signal was used to generate a mask of the region of interest (ROI). The ROI was used over a maximum intensity Z projection of GFP signal to quantify mean intensity and then moved to the background to measure it. Background was subtracted to the terminal's signal to get the final values. For statistical analysis, the fluorescence intensity at the terminals for each time point was modeled using a general linear mixed model, in which the replica number was treated as a random variable. Furthermore, the model incorporates a parameter that allows the adjustment of the variance. Subsequent analysis was conducted using the Bonferroni test.
Mitochondrial complexity index (MCI). The mitochondrial complexity index was examined in two ways: firstly, as a function of time point, and secondly, as a function of distance to the first branching point. In both instances, a linear mixed model was fitted, and the variable was transformed using the natural logarithm. Subsequently, a post hoc analysis with the Bonferroni test was conducted for the purpose of comparing the time points.
Varicosities girth. The data was fitted to a linear mixed model in which neurons were considered as a random variable and evaluated *a posteriori* with the Bonferroni test.
In all graphs, error bars indicate the standard error of the mean (SEM). Asterisks indicate statistically significant differences: * $p < 0.05$, ** $p < 0.01$, *** $p < 0.001$. Non-significant differences are not shown. Exact values for analyses and p values for contrasts are included in **Supplementary Tables 1 and 2**. The sample size (*n*) is indicated above symbols in graphs that have been statistically analyzed. The number of experiments performed is referred to as *N*.

Acknowledgements

We are indebted to members of the Ceriani lab for helpful discussions and to A. Liceri for the constant provision of fly food and help with fly work. We thank M. I. Farías for the help with the characterization of the APEX2 lines and A. H. Rossi and A. Ross from the Microscopy and Bioimaging Facility at Leloir Institute Foundation for the assistance and support in obtaining the

confocal microscopy images. We also thank Justin Blau for sharing *pdf*-RFP. Finally, we thank the members of NCMIR for training and discussions regarding EM sample preparation and analysis. Stocks obtained from the Bloomington Drosophila Stock Center (NIH P40OD018537) were used in this study.

Consent for Publication

Not applicable.

Funding

JII, MRC and CCR are supported by graduate fellowships from the Argentine Research Council for Science and Technology (CONICET). FJT holds a fellowship from the National Agency for the Promotion of Science, Technology and Innovation (Agencia I+D+i). JG and MFC are members of CONICET. This work was supported by the PICT2018-0995 (to MFC) from Agencia I+D+i, Argentina and by R01NS108934 (to Hdelal, ME and MFC). The funders had no role in study design, data collection and analysis, decision to publish, or preparation of the manuscript.

Availability of data and materials

All data generated or analyzed during this study are included in this published article and its supplementary information files. Any other data can be requested from the corresponding author.

Author contributions

Experimental design: JII, FJT, MRC, MFC, ME, ER, HOI
Data acquisition and analysis: JII, FJT, MRC, CCR, KK
Statistical analyses: CCR
Generation of transgenic lines: JII, CNH, ER, MFC
Algorithm development: FJT, CIP, MB
Manuscript writing and revision: JII, MRC, MFC, ER
Review & editing of the final version: All authors

Competing interests

The authors declare that they have no competing interests.

Ethics declarations and consent to participate

Not applicable.

Bibliography

1. Jabbur, M. L., Dani, C., Spoelstra, K., Dodd, A. N. & Johnson, C. H. Evaluating the Adaptive Fitness of Circadian Clocks and their Evolution. *J. Biol. Rhythms* **39**, 115 (2024).
2. Gliech, C. R. & Holland, A. J. Keeping track of time: The fundamentals of cellular clocks. *J. Cell Biol.* **219**, e202005136 (2020).
3. Reinhard, N. *et al.* Synaptic connectome of the *Drosophila* circadian clock. *bioRxiv* doi:https://doi.org/10.1101/2023.09.11.557222.
4. Abhilash, L., Ramakrishnan, A., Priya, S. & Sheeba, V. Waveform Plasticity under Entrainment to 12-h T-cycles in *Drosophila* melanogaster: Behavior, Neuronal Network, and Evolution. *J. Biol. Rhythms* **35**, 145–157 (2020).
5. Abruzzi, K. C. *et al.* RNA-seq analysis of *Drosophila* clock and non-clock neurons reveals neuron-specific cycling and novel candidate neuropeptides. *PLOS Genet.* **13**, e1006613 (2017).
6. Park, J. H. *et al.* Differential regulation of circadian pacemaker output by separate clock genes in *Drosophila*. *Proc. Natl. Acad. Sci.* **97**, 3608–3613 (2000).
7. Hofbauer, B. *et al.* The neuropeptide pigment-dispersing factor signals independently of Bruchpilot-labelled active zones in daily remodelled terminals of *Drosophila* clock neurons. *Eur. J. Neurosci.* **59**, 2665–2685 (2024).
8. Yoshii, T. *et al.* The neuropeptide pigment-dispersing factor adjusts period and phase of

Drosophila's clock. *J. Neurosci. Off. J. Soc. Neurosci.* **29**, 2597–2610 (2009).

9. Dissel, S. *et al.* The logic of circadian organization in *Drosophila*. *Curr. Biol. CB* **24**, 2257–2266 (2014).
10. Renn, S. C., Park, J. H., Rosbash, M., Hall, J. C. & Taghert, P. H. A pdf neuropeptide gene mutation and ablation of PDF neurons each cause severe abnormalities of behavioral circadian rhythms in *Drosophila*. *Cell* **99**, 791–802 (1999).
11. Stoleru, D., Peng, Y., Nawathean, P. & Rosbash, M. A resetting signal between *Drosophila* pacemakers synchronizes morning and evening activity. *Nature* **438**, 238–242 (2005).
12. Stoleru, D., Peng, Y., Agosto, J. & Rosbash, M. Coupled oscillators control morning and evening locomotor behaviour of *Drosophila*. *Nature* **431**, 862–868 (2004).
13. Grima, B., Chélot, E., Xia, R. & Rouyer, F. Morning and evening peaks of activity rely on different clock neurons of the *Drosophila* brain. *Nature* **431**, 869–873 (2004).
14. Fernández, M. P., Berni, J. & Ceriani, M. F. Circadian Remodeling of Neuronal Circuits Involved in Rhythmic Behavior. *PLOS Biol.* **6**, e69 (2008).
15. Gorostiza, E. A., Depetris-Chauvin, A., Frenkel, L., Pírez, N. & Ceriani, M. F. Circadian pacemaker neurons change synaptic contacts across the day. *Curr. Biol. CB* **24**, 2161–2167 (2014).
16. Depetris-Chauvin, A. *et al.* Adult-specific electrical silencing of pacemaker neurons uncouples molecular clock from circadian outputs. *Curr. Biol. CB* **21**, 1783–1793 (2011).
17. Sivachenko, A., Li, Y., Abruzzi, K. C. & Rosbash, M. The transcription factor Mef2 links the *Drosophila* core clock to Fas2, neuronal morphology, and circadian behavior. *Neuron* **79**, 281–292 (2013).
18. Herrero, A. *et al.* Coupling Neuropeptide Levels to Structural Plasticity in *Drosophila* Clock Neurons. *Curr. Biol. CB* **30**, 3154-3166.e4 (2020).
19. Lam, S. S. *et al.* Directed evolution of APEX2 for electron microscopy and proteomics. *Nat. Methods* **12**, 51 (2014).

20. Scheffer, L. K. *et al.* A connectome and analysis of the adult *Drosophila* central brain. *eLife* **9**, e57443.
21. Dorkenwald, S. *et al.* Neuronal wiring diagram of an adult brain. *Nature* **634**, 124–138 (2024).
22. Kremer, J. R., Mastronarde, D. N. & McIntosh, J. R. Computer visualization of three-dimensional image data using IMOD. *J. Struct. Biol.* **116**, 71–76 (1996).
23. Yasuyama, K. & Meinertzhagen, I. A. Synaptic connections of PDF-immunoreactive lateral neurons projecting to the dorsal protocerebrum of *Drosophila* melanogaster. *J. Comp. Neurol.* **518**, 292–304 (2010).
24. Shang, Y. *et al.* Short neuropeptide F is a sleep-promoting inhibitory modulator. *Neuron* **80**, 171 (2013).
25. Liang, X., Holy, T. E. & Taghert, P. H. A Series of Suppressive Signals within the *Drosophila* Circadian Neural Circuit Generates Sequential Daily Outputs. *Neuron* **94**, 1173-1189.e4 (2017).
26. Cao, G. & Nitabach, M. N. Circadian control of membrane excitability in *Drosophila* melanogaster lateral ventral clock neurons. *J. Neurosci. Off. J. Soc. Neurosci.* **28**, 6493–6501 (2008).
27. Feinberg, E. H. *et al.* GFP Reconstitution Across Synaptic Partners (GRASP) defines cell contacts and synapses in living nervous systems. *Neuron* **57**, 353–363 (2008).
28. Garcia, G. C. *et al.* Mitochondrial morphology provides a mechanism for energy buffering at synapses. *Sci. Rep.* **9**, 18306 (2019).
29. Rangaraju, V., Lauterbach, M. & Schuman, E. M. Spatially Stable Mitochondrial Compartments Fuel Local Translation during Plasticity. *Cell* **176**, 73-84.e15 (2019).
30. Nässel, D. R. & Zandawala, M. Hormonal axes in *Drosophila*: regulation of hormone release and multiplicity of actions. *Cell Tissue Res.* **382**, 233–266 (2020).
31. Im, S. H. & Taghert, P. H. PDF receptor expression reveals direct interactions between

circadian oscillators in *Drosophila*. *J. Comp. Neurol.* **518**, 1925–1945 (2010).

32. Vecsey, C. G. *et al.* Sleep deprivation impairs cAMP signalling in the hippocampus. *Nature* **461**, 1122–1125 (2009).
33. Klose, M., Kim, J. & Levitan, E. *Activity-Dependent Capture of Neuropeptide Vesicles Prepares Clock Neuron Synapses for Daily Release*. *bioRxiv : the preprint server for biology* (2023). doi:10.1101/2023.12.01.569590.
34. Wong, M. Y., Cavolo, S. L. & Levitan, E. S. Synaptic neuropeptide release by dynamin-dependent partial release from circulating vesicles. *Mol. Biol. Cell* **26**, 2466–2474 (2015).
35. Cao, G. *et al.* Genetically targeted optical electrophysiology in intact neural circuits. *Cell* **154**, 904–913 (2013).
36. Muraro, N. I. & Ceriani, M. F. Acetylcholine from Visual Circuits Modulates the Activity of Arousal Neurons in *Drosophila*. *J. Neurosci. Off. J. Soc. Neurosci.* **35**, 16315–16327 (2015).
37. Klose, M. K., Bruchez, M. P., Deitcher, D. L. & Levitan, E. S. Temporally and spatially partitioned neuropeptide release from individual clock neurons. *Proc. Natl. Acad. Sci.* **118**, e2101818118 (2021).
38. Prokop, A. & Meinertzhagen, I. A. Development and structure of synaptic contacts in *Drosophila*. *Semin. Cell Dev. Biol.* **17**, 20–30 (2006).
39. Sager, G. *et al.* Spatial and morphological organization of mitochondria across a connectome. 2024.08.21.608912 Preprint at https://doi.org/10.1101/2024.08.21.608912 (2024).
40. Petsakou, A., Sapsis, T. P. & Blau, J. Circadian Rhythms in Rho1 Activity Regulate Neuronal Plasticity and Network Hierarchy. *Cell* **162**, 823–835 (2015).
41. Duhart, J. M. *et al.* Circadian Structural Plasticity Drives Remodeling of E Cell Output. *Curr. Biol.* **30**, 5040-5048.e5 (2020).
42. Adebayo, M., Singh, S., Singh, A. P. & Dasgupta, S. Mitochondrial fusion and fission: The

fine-tune balance for cellular homeostasis. *FASEB J. Off. Publ. Fed. Am. Soc. Exp. Biol.* **35**, e21620 (2021).

43. de Goede, P., Wefers, J., Brombacher, E. C., Schrauwen, P. & Kalsbeek, A. Circadian rhythms in mitochondrial respiration. *J. Mol. Endocrinol.* **60**, R115–R130 (2018).
44. Sholl, D. A. Dendritic organization in the neurons of the visual and motor cortices of the cat. *J. Anat.* **87**, 387–406 (1953).
45. Schubert, F. K., Hagedorn, N., Yoshii, T., Helfrich-Förster, C. & Rieger, D. Neuroanatomical details of the lateral neurons of *Drosophila* melanogaster support their functional role in the circadian system. *J. Comp. Neurol.* **526**, 1209–1231 (2018).
46. Pyza, E. & Meinertzhagen, I. A. Daily rhythmic changes of cell size and shape in the first optic neuropil in *Drosophila* melanogaster. *J. Neurobiol.* **40**, 77–88 (1999).
47. Brand, A. H. & Perrimon, N. Targeted gene expression as a means of altering cell fates and generating dominant phenotypes. *Dev. Camb. Engl.* **118**, 401–415 (1993).
48. Gordon, M. D. & Scott, K. Motor control in a *Drosophila* taste circuit. *Neuron* **61**, 373–384 (2009).
49. Deerinck, T. J. *et al.* High-performance serial block-face SEM of non-conductive biological samples enabled by focal gas injection-based charge compensation. *J. Microsc.* **270**, 142 (2017).
50. Vincent, A. E. *et al.* Quantitative 3D Mapping of the Human Skeletal Muscle Mitochondrial Network. *Cell Rep.* **27**, 321 (2019).
51. Imbrosci, B., Schmitz, D. & Orlando, M. Automated Detection and Localization of Synaptic Vesicles in Electron Microscopy Images. *eNeuro* **9**, ENEURO.0400-20.2021 (2022).
52. clEsperanto/pyclesperanto_prototype. clEsperanto (2024).
53. Pinheiro, J., Bates, D., & R Core Team. nlme: Linear and Nonlinear Mixed Effects Models. 3.1-166 https://doi.org/10.32614/CRAN.package.nlme (1999).
54. Bates, D., Maechler, M., Bolker, B. & Walker, S. lme4: Linear Mixed-Effects Models using

‘Eigen’ and S4. 1.1-35.5 https://doi.org/10.32614/CRAN.package.lme4 (2003).

55. Brooks, M. *et al.* glmmTMB: Generalized Linear Mixed Models using Template Model Builder. (2024).

56. Lenth, R. V. *et al.* emmeans: Estimated Marginal Means, aka Least-Squares Means. (2024).

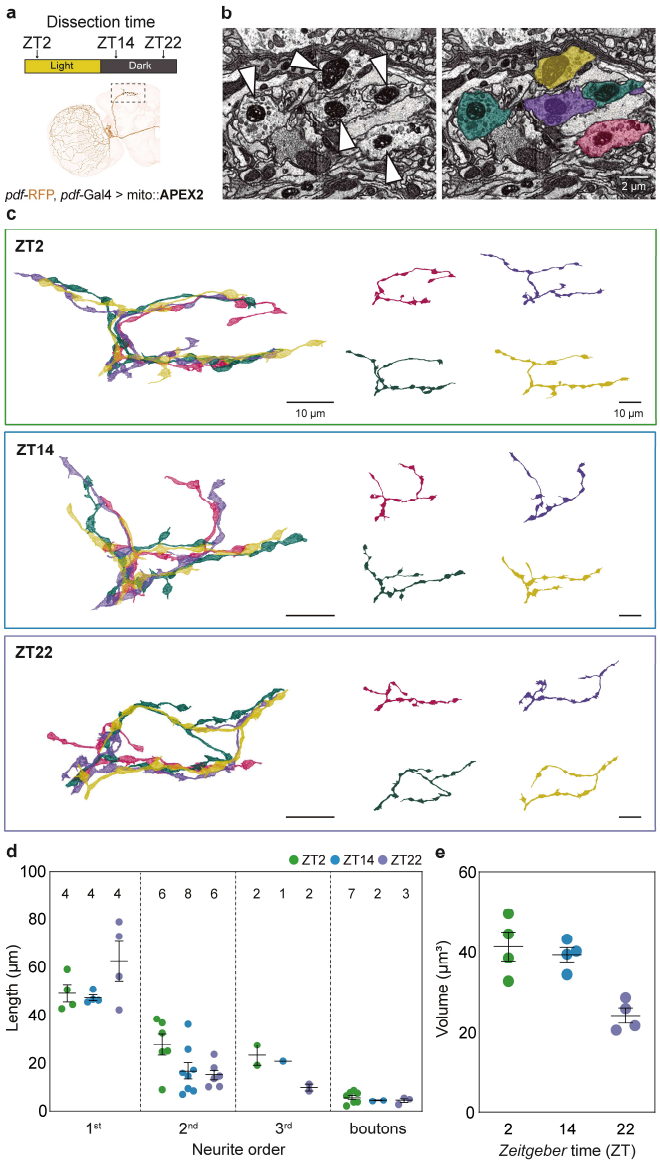

Figure 1. Segmentation and modeling of the s-LNvs. a, schematic diagram of the experimental setup. The fluorescent reporter (*pdf*-RFP) enabled identification of the s-LNv terminals region. mito::APEX2 along with DAB was employed to stain LNvs mitochondria for SBEM. **b**, labeled mitochondria (arrowheads) allowed identification of the neurons of interest. **c**, model after manual segmentation of the s-LNvs, displaying all of them together (left) or separated (right) at each time point. **d**, quantitation of the neurite length according to their order. Primary neurites were defined as the longest path from the initial branch point to the end of the neurite. The total number of neurites of each order is indicated at the top. **e**, quantitation of the total volume per neuron per time point. In all cases, error bars represent the standard error of the mean (SEM).

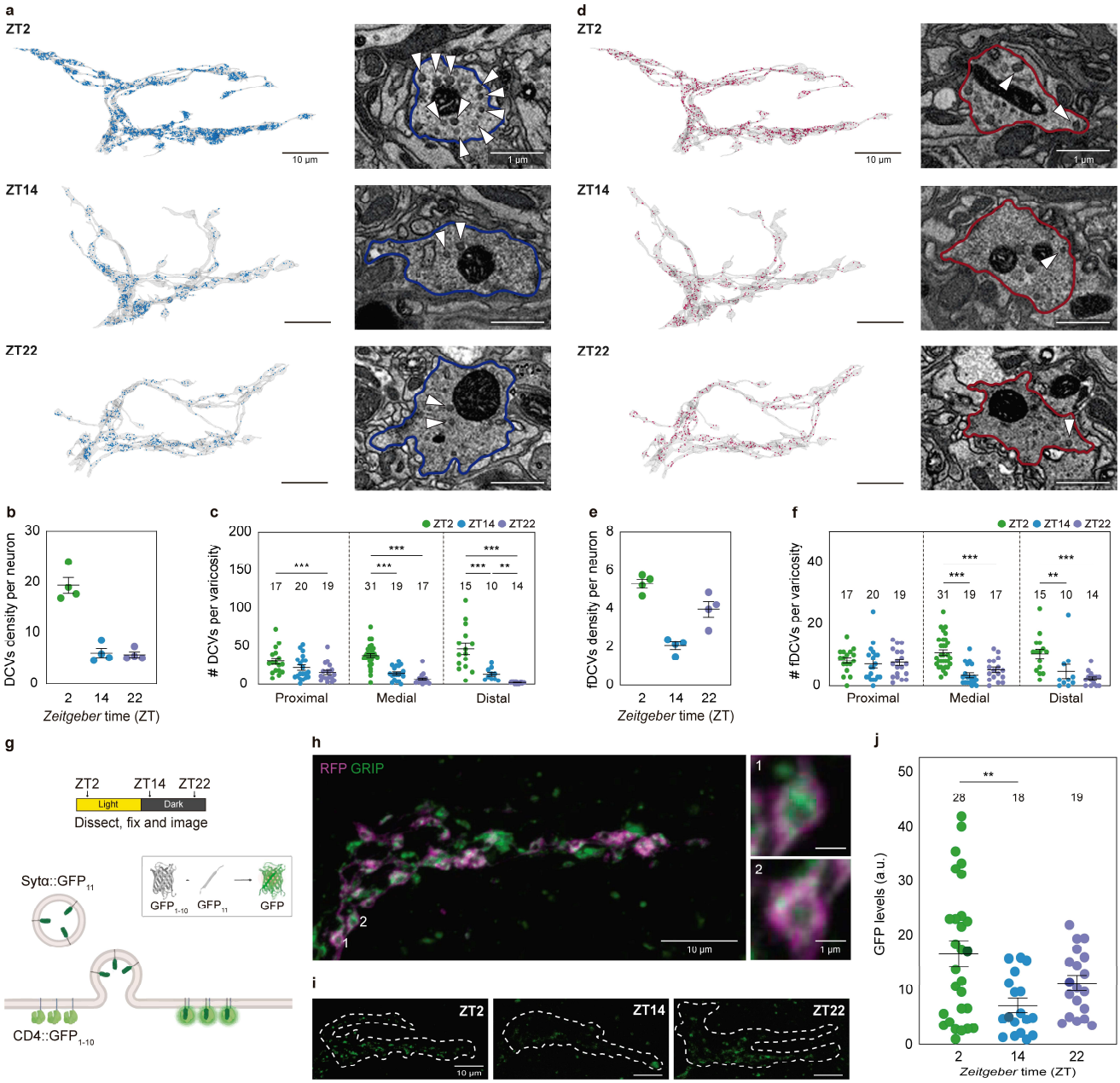

Figure 2. DCVs availability and fusion changes throughout the day. a, **d** segmented free DCVs (**a**) and fDCVs (**d**) in modeled neurons (left) and representative EM images (right, arrowheads) at each time point. **b**, **e** free DCV (**b**) and fDCV (**e**) density (as total number of DCVs/neuron volume) at each time point. **c**, **f** number of free DCVs (**c**) and fDCVs (**f**) per varicosity per time point; quantitation in proximal, medial and distal refers to thirds of the neuron defined by the length of its primary neurite. **g**, schematic diagrams of the experimental setup (top) and the logic of GFP reconstitution in the pre-synapse (GRIP, bottom). DCVs decorated with Sytα::GFP_{11} fuse to the membrane containing CD4::GFP_{1-10} to release their content. Reconstituted GFP highlights release sites. **h**, the projection of a Z stack of s-LNv terminals expressing *pdf*-RFP (to label structure) and GRIP acquired with an Airyscan confocal detector. Individual varicosities are shown in insets 1 and 2. **i**, representative confocal images of GRIP. **j**, Reconstituted GRIP at each time point. Each dot represents a brain. Darker symbols highlight the ones shown in **i**. *N* (number of experiments) = 2. n_1 = 13, 9, 9. n_2 = 15, 12, 10. In all graphs, error bars indicate the standard error of the mean (SEM). Asterisks indicate statistically significant differences: * $p < 0.05$, ** $p < 0.01$, *** $p < 0.001$. Non-significant differences are not shown. The sample size (*n*) is indicated above the symbols in each graph.

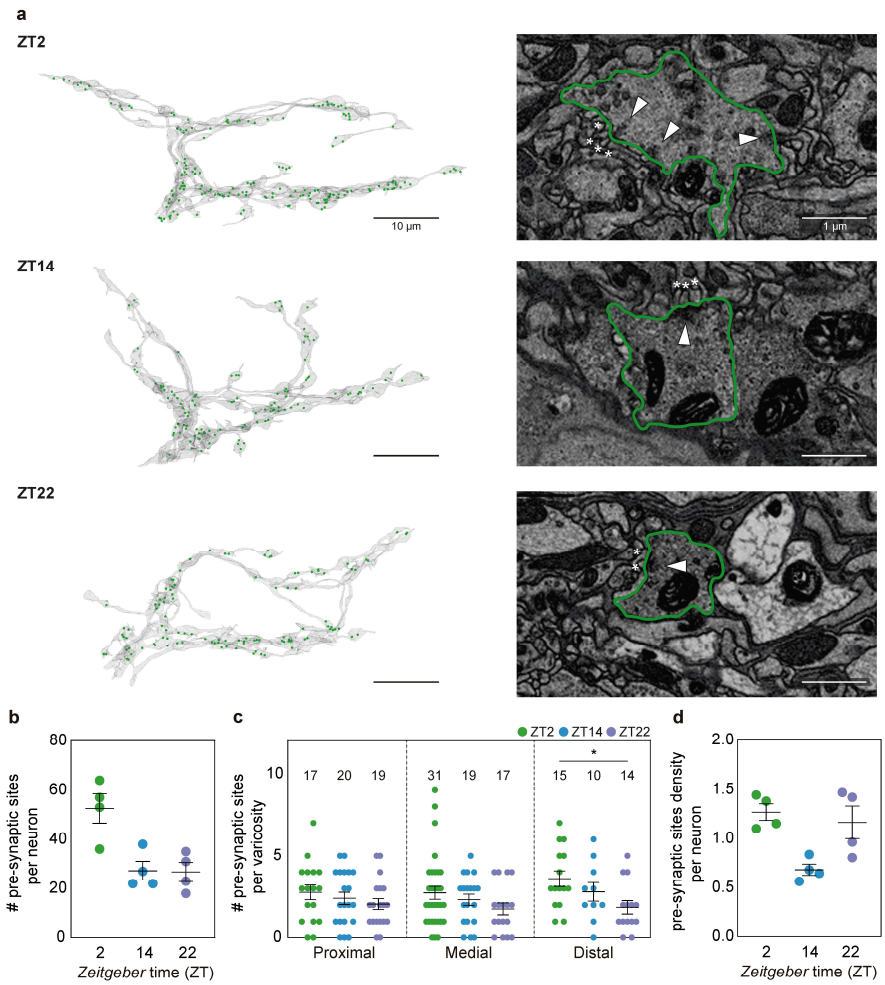

Figure 3. Pre-synaptic sites are more abundant in the morning. a, segmented pre-synaptic sites in modeled neurons (left) and in representative EM images (right, arrowheads). Asterisks indicate putative post-synapses. **b**, total number of pre-synaptic sites per neuron at each time point. **c**, number of pre-synaptic sites per varicosity per terminal section at each time point as defined in 2c. **d**, pre-synaptic site density (total number of pre-synaptic sites/neuronal volume) at each time point. In all graphs, error bars indicate the standard error of the mean (SEM). Asterisks indicate statistically significant differences: * $p < 0.05$, ** $p < 0.01$, *** $p < 0.001$. Non-significant differences are not shown. The sample size (*n*) is indicated above the symbols in each graph.

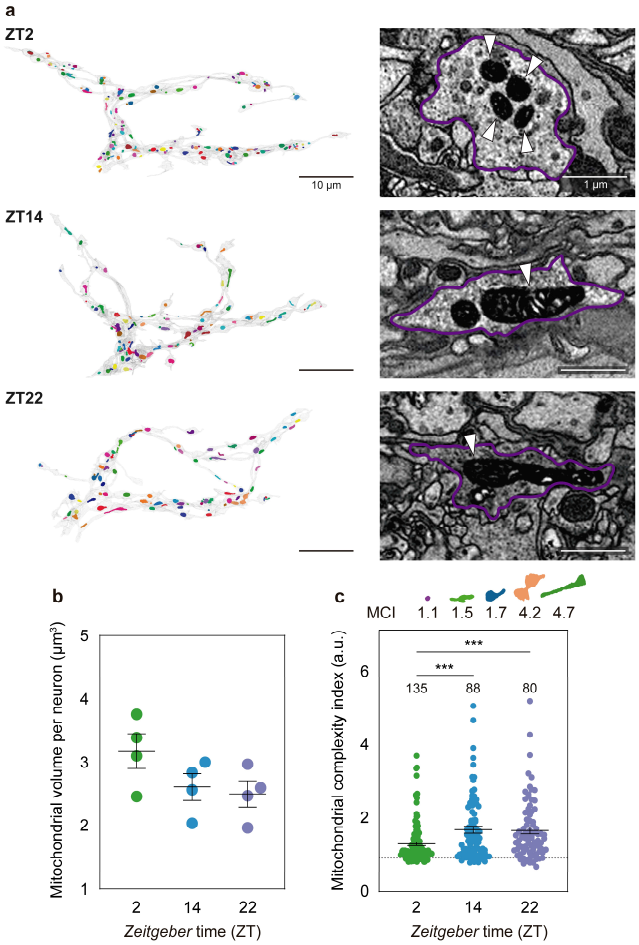

Figure 4. Mitochondrial morphology changes along the day. a, segmented mitochondria in modeled neurons (left) and in representative EM images (right) at each time point. **b**, total mitochondrial volume per neuron at each time point. **c**, mitochondrial complexity index (MCI) per time point. Each symbol represents one mitochondrion. In all graphs, error bars indicate the standard error of the mean (SEM). Asterisks indicate statistically significant differences: * $p < 0.05$, ** $p < 0.01$, *** $p < 0.001$. Non-significant differences are not shown. The sample size (*n*) is indicated above the symbols in each graph.

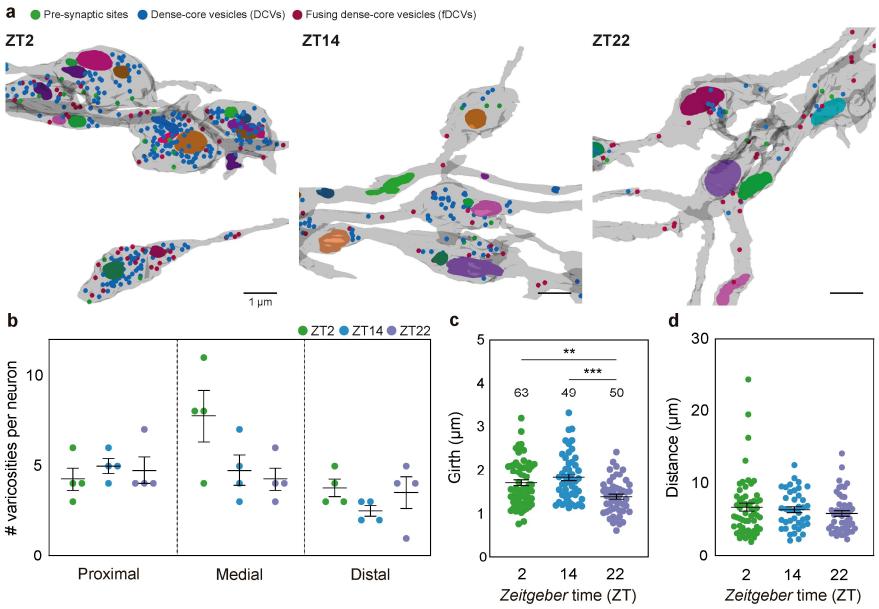

Figure 5. Varicosities show structural and functional plasticity. a, representative modeled varicosities observed at different time points. Individual mitochondria are labeled in different colors. **b**, total number of varicosities per neuron and terminal section as in **Figure 2c**. **c**, varicosities girth at each time point. **d**, distance between varicosities at each time point. In all graphs, error bars indicate the standard error of the mean (SEM). Asterisks indicate statistically significant differences: * $p < 0.05$, ** $p < 0.01$, *** $p < 0.001$. Non-significant differences are not shown. The sample size (*n*) is indicated above the symbols in each graph.